The Collapse and Expansion of Liquid-filled Elastic Channels and Cracks

Fanbo Meng[†], Jiexi Huang[†] and M. D. Thouless[†,‡]
[†]*Department of Mechanical Engineering*
[‡]*Department of Materials Science & Engineering*
University of Michigan, Ann Arbor, MI 48109, USA

Abstract

The rate at which fluid drains from a collapsing channel or crack depends on the interaction between the elastic properties of the solid and the fluid flow. The same interaction controls the rate at which a pressurized fluid can flow into a crack. In this paper, we present an analysis for the interaction between the viscous flow and the elastic field associated with an expanding or collapsing fluid-filled channel. We first examine an axisymmetric problem for which a completely analytical solution can be developed. A thick-walled elastic cylinder is opened by external surface tractions, and its core is filled by a fluid. When the applied tractions are relaxed, a hydrostatic pressure gradient drives the fluid to the mouth of the cylinder. The relationship between the change in dimensions, time and position along the cylinder is given by the diffusion equation, with the diffusion coefficient being dependent on the modulus of the substrate, the viscosity of the fluid, and the ratio of the core radius to the exterior radius of the cylinder.

The second part of the paper examines the collapse of elliptical channels with arbitrary aspect ratios, so as to model the behavior of fluid-filled cracks. The channels are opened by a uniaxial tension parallel to their minor axes, filled with a fluid, and then allowed to collapse. The form of the analysis follows that of the axisymmetric calculations, but is complicated by the fact that the aspect ratio of the ellipse changes in response to the local pressure. Approximate analytical solutions in the form of the diffusion equation can be found for small aspect ratios. Numerical solutions are given for more extreme aspect ratios, such as those appropriate for cracks. Of particular note is that, for a given cross-sectional area, the rate of collapse is slower for larger aspect ratios. With minor modifications to the initial conditions and the boundary conditions, the analysis is also valid for cracks being opened by a pressurized fluid.

Keywords: nano-channels; cracks; fluid flow; elastic deformation; solid-fluid interactions

July 1, 2015

1 Introduction

Nano-fluidic channels fabricated by cracking a thin film supported on an elastic substrate are used for biological applications including DNA and chromatin analyses [1, 2, 3, 4], cell patterning [5, 6, 7], and biomimetic systems [8]. The fabrication of this type of nanochannel is fairly easy and cost-effective: an array of parallel channels is created by applying tension to a layered structure. This concept has been greatly enhanced by the development of techniques for controlled cracking, in which micro-features are used to initiate and propagate cracks at desired locations [9, 10], so that there are many identical channels on one substrate. After fabrication, the channels can be reversibly opened and closed by the application and relaxation of an applied tensile strain. In particular, opening the channels by applying a strain allows single strands of DNA and chromatin to be loaded into the channels. Subsequent narrowing of the channels by relaxing the strain provides the confinement that, accompanied by nano-scale squeezing flow, can linearize the DNA and chromatin [4]. This present work was motivated by the need to understand the interaction between a collapsing elastic channel and a fluid contained within it, so as to help develop the optimal design of such channels and the operation of them.

Since the channels are nano-scale, three-dimensional structures beneath a surface, characterization of their shape and size is difficult. Scanning-electron microscopy and laser confocal-microscopy have been used to characterize surface cracks [1, 4, 10]. The results provide some reference for the shape and size of tunneling cracks, but don't reflect the real profiles of liquid-filled nanochannels. Electrical-impedance methods have been used to determine the average cross-sectional area of nanochannels [3, 4]. The accuracy of these results is greatly affected by the choice of model used to in-

terpret them, and by ion depletion that can occur during the experiments. Photo-activated localization microscopy has been used to perform super-resolution imaging of nanochannels [11]. While this technique provides high-resolution images, it is limited to two-dimensions, and cannot track the time-dependent narrowing process, because it takes an average of signals over time. Hence, the need to use computational methods to understand the time-dependent narrowing of fluid-filled nanochannels in elastic substrates.

Existing analyses for flow in elastic channels fall into two groups: (i) flow driven by prescribed wall movements, and (ii) collapse of an elastic wall responding to established flow. Analyses for the first group, where flow is driven by the movement of a channel wall, were developed for studies of peristaltic transport of biofluids [12, 13, 14, 15] and membrane-activated microfluidic pumps [16, 17, 18, 19]. The elasticity of the channel walls in these studies was neglected, and flow was assumed to be driven by prescribed displacements. In the analyses for the second group of flow-induced collapse [20, 21], the fluid flow was prescribed by steady-state flow being established upstream and downstream. A final balanced state of the collapsed channel was solved by iterating the movement of the interface at different positions along the tube until the steady-state configuration was achieved. Since only steady-state conditions were considered, evolution of the channel profile was not addressed. Our analysis differs from these existing analyses in that it studies the transient process of channel narrowing by solving the stress field for an elastic channel, and coupling the stresses to gradients in the fluid pressure and the resultant flow. Time-dependent channel profiles naturally evolve from this approach.

This paper consists of two parts. In the first part, we present an analytical result

for a thick-walled axisymmetric tube that is expanded by external tensile tractions, filled with a liquid, and then collapses when the external tractions are removed. This provides insight into the mechanics of the process, and shows how the channel narrows in a non-uniform fashion, starting from one end, and proceeding towards the center of the tube. In the second part of the paper, we repeat this process to analyze the collapse of elliptical channels after relaxation of a uniaxial tension. While the equations for this second portion of the paper are developed analytically, they have to be solved numerically. However, they provide more general solutions, and a more realistic approximation to the experimental configuration that originally motivated the study.

2 Axisymmetric tubes

To provide insight into how a fluid-filled elastic channel collapses, we first develop an analytical result for the axisymmetric problem of a cylindrical elastic tube. The tube is made from an incompressible elastic material with a modulus of E. The fluid is also incompressible with a visocity of η. The inner radius of the tube is R_1, and the outer radius is R_2. These have values R_{1_o} and R_{2_o} when the cylinder is fully relaxed. It is assumed in the following calculations that changes in R_1 and R_2 are always small compared to R_{1_o} and R_{2_o}. The tube has a half length of L, which is much greater than the other two dimensions. Since the problem is symmetric about the center of the tube, half of the geometry is considered, as shown in Fig. 1(a). Cylindrical coordinates of r, θ, z are employed. The radial and hoop stresses in a thick-walled

tube are described by the Lamé equations:

$$\sigma_{rr} = C_1 + C_2/r^2$$
$$\sigma_{\theta\theta} = C_1 - C_2/r^2 \tag{1}$$

where C_1 and C_2 are constants which can be calculated from the boundary conditions for the particular problem being considered, and r is the radius at any point.

The analysis is performed in several steps. First the tube is expanded by the application of a uniform traction, σ_o, on the external surface as shown in Fig. 1(b). The radius of the inner core is calculated under these applied tractions. In particular, the volume change of the core for an element of length δL is calculated. It is assumed that fluid flows into the cylinder under these conditions, so that it fills the core at the ambient pressure. The remote tractions are then released, causing the tube to exert a pressure P_o on the fluid on the core. This pressure is found by determining the radial compressive tractions that would need to be applied to the internal surface of the cylinder core to produce the volume change calculated above, subject to an additional set of assumptions that the axial displacements of the cylinder are all planar, and there is no net axial force acting on the tube and fluid. (In practice, this is done in two steps: a plane-strain calculation with the internal radial compressive tractions of P_o, followed by the application of a uniform axial tensile load of $\pi P_o R_{1_o}^2$. P_o is found by equating the total volume change associated with these calculations to the volume change induced by the external tractions, σ_o.)

Once the initial pressure away from the exit of the tube has been calculated, the fluid flow is calculated by assuming (i) incompressible Poiseulle flow to the exit where the pressure of the fluid is at ambient pressure, (ii) compatibility between the local

fluid pressure and the local volume of the core, (iii) plane displacements, and (iv) no net axial load. These calculations are demonstrated analytically for the cylinder to illustrate the process. The same concepts form the basis of the subsequent calculations for elliptical channels.

2.1 Initial expansion of the tube

The tube is initially expanded by applying uniform tensile tractions, σ_o, to the outer surface of the tube. Consider a thin slice of the cylinder of length δL, opening under plane-displacement conditions[1]. The problem can be analyzed by superposition of the solutions to two problems: (i) plane-strain deformation under exterior radial tractions, and (ii) deformation from a uniform tensile load to satisfy the condition of no net axial force.

The boundary conditions for the first, plane-strain problem are

$$\begin{aligned} \sigma_{rr} &= \sigma_o \quad (\text{at } r = R_{2_o}), \\ \sigma_{rr} &= 0 \quad (\text{at } r = R_{1_o}), \\ &\text{and } \varepsilon_{zz} = 0 \, . \end{aligned} \tag{2}$$

Solving the Lamé equations (Eqn. 1) with these boundary conditions, we find that $C_1 = \rho_o^2 \sigma_o / (\rho_o^2 - 1)$ and $C_2 = -\rho_o^2 \sigma_o R_{1_o}^2 / (\rho_o^2 - 1)$, where $\rho_o = R_{2_o}/R_{1_o}$. The axial stress induced in plane strain is found from Hooke's Law, with $\epsilon_{zz} = 0$. The resultant

[1] This is the assumption that plane sections perpendicular to the axis of the channel remain plane, and is enforced with the additional constraint of no net axial load. It is this second requirement that distinguishes plane-displacement boundary conditions from plane-strain conditions.

stresses are

$$\sigma_{rr} = \frac{\rho_o^2}{\rho_o^2 - 1}\left(1 - \frac{R_{1_o}^2}{r^2}\right)\sigma_o \ ,$$
$$\sigma_{\theta\theta} = \frac{\rho_o^2}{\rho_o^2 - 1}\left(1 + \frac{R_{1_o}^2}{r^2}\right)\sigma_o \ ,$$
$$\sigma_{zz} = \frac{\rho_o^2}{\rho_o^2 - 1}\sigma_o \ . \tag{3}$$

Integrating the axial stress over the cross-section of the tube gives a net axial tensile load of

$$F_z = \pi R_{1_o}^2 \rho_o^2 \sigma_o \ , \tag{4}$$

resulting from this first step in the calculations. To ensure a plane-displacement solution with no net axial tension, the stress and strain fields resulting from the application of a uniform compressive load of this magnitude need to be added to the previous solutions. This results in an additional stress component of

$$\sigma_{zz} = -\frac{\rho_o^2}{\rho_o^2 - 1}\sigma_o \ , \tag{5}$$

with all the other additional stresses being zero. Therefore, by linear superposition, the stress and strain fields resulting from the channel opening process are:

$$\sigma_{rr} = \frac{\rho_o^2}{\rho_o^2 - 1}\left(1 - \frac{R_{1_o}^2}{r^2}\right)\sigma_o \ ,$$
$$\sigma_{\theta\theta} = \frac{\rho_o^2}{\rho_o^2 - 1}\left(1 + \frac{R_{1_o}^2}{r^2}\right)\sigma_o \ ,$$
$$\sigma_{zz} = 0 \ ,$$
$$\varepsilon_{rr} = \frac{\rho_o^2}{2(\rho_o^2 - 1)}\left(1 - \frac{3R_{1_o}^2}{r^2}\right)\frac{\sigma_o}{E} \ ,$$
$$\varepsilon_{\theta\theta} = \frac{\rho_o^2}{2(\rho_o^2 - 1)}\left(1 + \frac{3R_{1_o}^2}{r^2}\right)\frac{\sigma_o}{E} \ ,$$
$$\varepsilon_{zz} = -\frac{\rho_o^2}{\rho_o^2 - 1}\frac{\sigma_o}{E} \ . \tag{6}$$

It transpires that this solution is identical to what would have been obtained with an assumption of plane stress along the axis of the cylinder. However, the full set of calculations has been presented, because this equivalence does not generally hold, and a simple calculation illustrates the concept that is necessary for the elliptical calculations that follow.

The volume of the core of an element of the cylinder of length δL_o is given by $V_o = \pi R_{1_o}^2 \delta L_o$. The change in volume of the element is given by

$$\frac{\Delta V}{V_o} = 2\frac{\Delta R_1}{R_{1_o}} + \frac{\Delta \delta L}{\delta L_o} = 2\epsilon_{\theta\theta}|_{r=R_1} + \epsilon_{zz}|_{r=R_1}, \tag{7}$$

where

$$\begin{aligned} \epsilon_{\theta\theta}|_{r=R_1} &= 2\frac{\rho_o^2}{\rho_o^2 - 1}\frac{\sigma_o}{E}\ , \\ \epsilon_{zz}|_{r=R_1} &= -\frac{\rho_o^2}{\rho_o^2 - 1}\frac{\sigma_o}{E}\ . \end{aligned} \tag{8}$$

This can be written as

$$\frac{\Delta V}{V_o} = 3\frac{\rho_o^2}{\rho_o^2 - 1}\frac{\sigma_o}{E}. \tag{9}$$

2.2 Relaxation of the applied tractions

The next step in the calculations is to compute the initial state of the cylinder and fluid immediately after the applied tractions are removed, but before any fluid can begin to flow out of the core. Since the fluid is incompressible, volume must be conserved. This means that if the radius of the core changes instantaneously upon removal of the external tractions, the length of the tube must increase by a corresponding amount. The unknown parameter that needs to be calculated is the initial

pressure in the fluid after the external tractions have been removed, P_o. This is calculated by determining the change in the volume of the core if the cylinder supports an internal pressure P_o, assuming plane-displacement conditions and no net axial force on the system[2], and equating this change in volume to that given by Eqn. 9. The details of the calculation are described below, since the steps are identical to those that follow for the more complicated case of an elliptical channel.

As described in the previous section, the solutions to the plane-displacement problem can be analyzed using linear superposition of two problems: a plane-strain problem, and a problem with a uniform axial stress. The plane-strain problem is solved using the following boundary conditions:

$$\begin{aligned} \sigma_{rr} &= 0 \quad (\text{at } r = R_{2_o}), \\ \sigma_{rr} &= -P_o \quad (\text{at } r = R_{1_o}), \\ &\text{and } \varepsilon_{zz} = 0 \, . \end{aligned} \tag{10}$$

The Lamé equations and Hooke's Law can be used with these boundary conditions

[2]The net axial force on any section must be zero since there is no fluid pressure at the outlet and there are no surface tractions on the ends of the cylinder. However, since the core supports a hydrostatic pressure, the solid material must support an equivalent tensile force. This tensile force develops in the solid as a result of shear stresses at the solid/fluid interface associated with the flow of the fluid.

to show that the corresponding stresses and strains are

$$\begin{aligned}
\sigma_{rr} &= \frac{P_o}{\rho_o^2 - 1}\left(1 - \frac{R_{2_o}^2}{r^2}\right) , \\
\sigma_{\theta\theta} &= \frac{P_o}{\rho_o^2 - 1}\left(1 + \frac{R_{2_o}^2}{r^2}\right) , \\
\sigma_{zz} &= \frac{P_o}{\rho_o^2 - 1} , \\
\varepsilon_{rr} &= -\frac{3P_o}{2E(\rho_o^2 - 1)}\frac{R_{2_o}^2}{r^2} , \\
\varepsilon_{\theta\theta} &= \frac{3P_o}{2E(\rho_o^2 - 1)}\frac{R_{2_o}^2}{r^2} , \\
\varepsilon_{zz} &= 0 .
\end{aligned} \tag{11}$$

Two components need to be added to the axial stress given above to ensure both no net axial force and plane-displacement conditions. The first is a compressive force of magnitude $-\pi R_{1_o}^2 P_o$ to negate the effect of the axial stress σ_{zz} in Eqn. 11. The second is a tensile force of magnitude $\pi R_{1_o}^2 P_o$ to balance the hydrostatic pressure within the fluid. Obviously, both of these cancel, leaving the stress and strains of Eqn. 11 as the full solution for the second part of the problem.

The change in the volume of the core associated with this stress state can be calculated using Eqn. 7 and the strains at $r = R_1$:

$$\begin{aligned}
\epsilon_{\theta\theta}|_{r=R_1} &= \frac{3\rho_o^2}{2(\rho_o^2 - 1)}\frac{P}{E} , \\
\epsilon_{zz}|_{r=R_1} &= 0.
\end{aligned} \tag{12}$$

This volume change is given by

$$\frac{\Delta V}{V_o} = \frac{3P}{E}\frac{\rho_o^2}{\rho_o^2 - 1}. \tag{13}$$

Equating this equation to Eqn. 9, it can be seen that the initial pressure in the core, P_o, must be equal to σ_o. This provides the initial hydrostatic pressure in the core of an incompressible elastic cylinder, before any flow out of the ends can occur, and is the starting point for the flow calculations of the next section. Again, this simple result is a feature of the cylindrical symmetry assumed. It doesn't hold for the general case of elliptical channels that will be considered later.

2.3 Viscous flow of the core

As shown above, upon relaxation of the external tractions, the fluid in the core develops a hydrostatic pressure of $P_o = \sigma_o$. The difference between this pressure and the ambient pressure will cause the fluid to flow to the exit of the tube. In the calculations that follow, it has been assumed that there is no slip at the interface between the inner surface of the tube and the fluid, there is continuity of stresses and displacements in the radial direction across the interface, the cylinder deforms under plane-displacement conditions, there is no net axial force on the tube and fluid, and there are only small perturbations on the radius of the core.

Fluid flow initiates at the ends of the tube, where the pressure gradient is greatest. Once the fluid flows out of an element, the cylinder contracts and the local pressure, P, decreases. The relationship between the local radius of the core, R_1, and the local pressure can be calculated using the Lamé equations and Hooke's Law, following the approach and assumptions of the previous section (see Eqn. 12):

$$\frac{\partial P(z,t)}{\partial z} = \frac{2E}{3R_{1_o}} \frac{(\rho_o^2 - 1)}{\rho_o^2} \frac{\partial R_1(z,t)}{\partial z} \ . \tag{14}$$

If it is assumed that the flow along the length of the tube can be described by Poiseulle flow, and that the strains are relatively small, so $R_1 \approx R_{1_o}$, the volumetric flow rate is given by

$$\dot{Q}(z,t) = -\frac{\pi R_{1_o}^4}{8\eta}\frac{\partial P(z,t)}{\partial z} \ , \tag{15}$$

where z is the axial distance along the cylinder measured from the end of tube. For an incompressible fluid, conservation of mass requires conservation of volume, so that

$$2\pi R_{1_o}\frac{\partial R_1}{\partial t} = -\frac{\partial \dot{Q}(z,t)}{\partial z} \ . \tag{16}$$

Equations 14 through 16 can then be combined to give the governing equation for fluid flow in the cylinder:

$$\frac{\partial R_1}{\partial t} = \frac{E R_{1_o}^2}{24\eta}\frac{(\rho_o^2 - 1)}{\rho_o^2}\frac{\partial^2 R_1}{\partial z^2} \ . \tag{17}$$

Equation 17 can be normalized using the non-dimensional parameters $\tau = Et/\eta$, $\psi = R_1/R_{1_o}, \zeta = (L_o - z)/R_{1_o}$, where R_1 is the current radius of the core, R_{1_o} is the original (fully-relaxed) radius of the core, and L_o is the original half length of the cylinder. The normalized form of the governing equation is given by

$$\frac{\partial \psi}{\partial \tau} = \rho^* \frac{\partial^2 \psi}{\partial \zeta^2}, \tag{18}$$

where

$$\rho^* = (\rho_o^2 - 1)/24\rho_o^2 \ .$$

The radius of inner surface is a function of axial location and time: $\psi = \psi(\zeta, \tau)$. The governing equation is in the form of the diffusion equation. For an infinitely long tube, the solution is given by

$$\psi(\zeta,\tau) = 1 + \Delta\psi^{max} \ \mathrm{erf}\left(\frac{\zeta}{2\sqrt{\rho^*\tau}}\right) \ , \tag{19}$$

where erf is the error function, and

$$\Delta\psi^{max} = \psi(\zeta, 0) - 1 = \sigma_o/16E\rho^*$$

corresponds to the difference between the radius of the fully-relaxed core and the radius of the core immediately after the applied tractions have been removed. The solution for an infinitely long, very thick tube with $\sigma_o/E = 0.01$ is presented in Fig. 2, and a schematic sketch showing how the profile of the cylinder changes as the fluid flows out of it is given in Fig. 3.

An equivalent form of Eqn. 19 is:

$$\frac{\Delta\psi}{\Delta\psi^{max}} = \text{erf}\left(\frac{\zeta}{2\sqrt{\rho^*\tau}}\right) , \tag{20}$$

where $\Delta\psi/\Delta\psi^{max}$ is the relative collapse of the core. If we define the collapse front as being the point at which $\Delta\psi/\Delta\psi^{max} = 0.5$, we can use Eqn. 20 to show that the location of this front is given by

$$\zeta_{0.5} = 0.954\sqrt{\rho^*\tau} . \tag{21}$$

Since ρ^* increases with wall thickness, up to an asymptotic limit of 1/24, it can be seen that the collapse front travels faster in systems with thicker elastic walls, up to a limit of

$$\frac{d\zeta_{0.5}}{d\tau} = 0.097\tau^{-1/2} \tag{22}$$

for very thick cylinders.

The solution to the diffusion equation for finite domains can also be found in standard text-books as a series solution [22]. Equation 18 can be solved with the

following boundary and initial conditions:

$$\psi(0,\tau) = 1, \text{ for } \tau > 0$$
$$\psi(2L_o/R_{1o},\tau) = 1, \text{ for } \tau > 0$$
$$\psi(\zeta,0) = 1 + \Delta\psi^{\max} . \tag{23}$$

This results in the solution

$$\psi = \left[\frac{4\Delta\psi^{\max}}{\pi}\Sigma_{n=0}^{\infty}\frac{1}{2n+1}e^{-\frac{\rho^*(2n+1)^2\pi^2\tau}{(2L_o/R_{1_o})^2}}\sin\frac{(2n+1)\pi\zeta}{2L_o/R_{1o}}\right] + 1 , \tag{24}$$

which has been added to Fig. 2, for a value of $L_o/R_{1_o} = 1000$.

3 Elliptical channels

Channels formed by cracking a sandwich layer can be modeled as an elliptical core in an infinite elastic body, since the channel width and depth are much smaller than the crack spacing and the thickness of the substrate [4, 10]. In this section, we analyze the behavior of a fluid-filled core that has, in the undeformed state, a major radius of a_o and a minor radius of b_o. The half length of the channel is L_o, which is much larger than either a_o or b_o. The elastic body is made of an incompressible elastic material with a modulus of E, and the fluid is incompressible with a viscosity of η.

The analysis is very similar to that presented in the previous case of an axisymmetric tube, except that the channel is opened by applying a remote uniaxial tension, σ_o, in the direction of the minor axis of the cylinder. While the channel is held in the opened state, it is filled with fluid. The applied tension is then relaxed to develop a pressure in the fluid. This pressure then drives the fluid out of the exit, until the channel returns to its original relaxed state. The process is depicted in Fig. 4, where

a quarter of the model is shown, reflecting the symmetry of the problem.

The general solution for stresses in an infinite plate with an elliptical hole is provided by Inglis [23]. Cartesian coordinates with x and y aligned with the major and minor radii, respectively, are transformed to curvilinear coordinates α, β by

$$x = \sqrt{{a_o}^2 - {b_o}^2}\cosh\alpha\cos\beta\ ,$$
$$y = \sqrt{{a_o}^2 - {b_o}^2}\sinh\alpha\sin\beta\ . \tag{25}$$

The z-axis is in the longitudinal direction pointing from the center to the exit. In this coordinate system, constant values of α correspond to ellipses with the same aspect ratio as the core, and the surface of the elliptical hole being defined by $\alpha = \alpha_o = \tanh^{-1}(b_o/a_o)$. Constant values of β correspond to lines that are orthogonal to these ellipses, with $0 \leq \beta < 2\pi$. The stress and displacement fields, and the corresponding shape changes, can be calculated for different boundary conditions. However, in contrast to the axisymmetric case, the calculations for the opening and closing of an elliptical channel are complicated by shape changes; these are addressed in the following sections.

3.1 Opening of the elliptical channel

The first set of calculations were conducted for the opening of the channel when the elastic body is subjected to a uniaxial tension, as shown in Fig. 4(b). As with the axisymmetric problem, the calculations were done under the assumption of plane-displacements perpendicular to the longitudinal axis of the channel. This required a plane-strain calculation to be done first, with boundary conditions of a remote tension, σ_o, in the direction of the minor axis, and zero tractions along the interior

surface of the ellipse. The stresses are given by Inglis [23]:

$$\begin{aligned}
\sigma_{\alpha\alpha} = -\sigma_o \Big\{ & 2e^{2\alpha_0} \left[1 - \cosh(2\alpha - 2\alpha_0)\right] \cos(4\beta) \\
& + 2e^{2\alpha_0} \left[\cosh(4\alpha - 2\alpha_0) + 3\cosh(2\alpha_0) - 4\cosh(2\alpha)\right] \cos(2\beta) \\
& + 4\cosh(2\alpha_0)\sinh(2\alpha) - 2\sinh(4\alpha) - 3e^{-2\alpha+4\alpha_0} - e^{2\alpha} + 4e^{2\alpha_0} \\
& - e^{2\alpha} - 2e^{-2\alpha} - 4e^{2\alpha_0} \Big\} \left\{ 8 \left(\cosh 2\alpha - \cos 2\beta\right)^2 \right\}^{-1} \ , \\
\sigma_{\beta\beta} = \sigma_o \Big\{ & -2e^{2\alpha_0} \left[1 + \cosh(2\alpha - 2\alpha_0)\right] \cos(4\beta) \\
& + 2e^{2\alpha_0} \left[\cosh(4\alpha - 2\alpha_0) + 3\cosh(2\alpha_0) + 8e^{-2\alpha} - 4e^{2\alpha-2\alpha_0} + 4e^{-2\alpha-2\alpha_0}\right] \cos(2\beta) \\
& + 4\cosh(2\alpha_0)\sinh(2\alpha) - 2\sinh(4\alpha) - 3e^{-2\alpha+4\alpha_0} - 2e^{2\alpha_0-4\alpha} \\
& - 2e^{-2\alpha} + 2e^{2\alpha_0-4\alpha} \Big\} \left\{ 8 \left(\cosh 2\alpha - \cos 2\beta\right)^2 \right\}^{-1} \ . \qquad (26)
\end{aligned}$$

The changes in the major and minor radii under these conditions can also be found from Ref. [23]:

$$\begin{aligned}
\Delta a_1 &= -\frac{3\sigma_o}{4E} a_o \ , \\
\Delta b_1 &= \frac{3\sigma_o}{4E} \left(2a_o + b_o\right) \ . \qquad (27)
\end{aligned}$$

Finally, the use of Hooke's law with the stresses of Eqn. 26, under plane-strain conditions, gives the axial stress:

$$\sigma_{zz}(\alpha, \beta) = \frac{\sigma_o}{2} \left(-e^{2\alpha_o} + \frac{(e^{2\alpha_o} + 1)\sinh 2\alpha}{\cosh 2\alpha - \cos 2\beta} \right) \ . \qquad (28)$$

The second step is to apply a uniform axial stress to negate the axial force induced by the plane-strain conditions, leaving plane-displacement conditions. The average stress induced by the plane-strain conditions for any value of α can be found by

integrating $\sigma_{zz}(\alpha,\beta)$ from Eqn. 28 with respect to β, over the interval $0 \le \beta \le \pi/2$:

$$\begin{aligned}\bar{\sigma}_{zz}(\alpha) &= \frac{1}{\pi/2}\int_0^{\pi/2} \sigma_{zz}(\alpha,\beta)d\beta \\ &= \frac{1}{\pi/2}\frac{\sigma_o}{2}\int_0^{\pi/2}\left(-e^{2\alpha_o} + \frac{(e^{2\alpha_o}+1)\sinh 2\alpha}{\cosh 2\alpha - \cos 2\beta}\right)d\beta \ . \end{aligned} \tag{29}$$

Using a standard table of integrals [24], this can be shown to be given by

$$\bar{\sigma}_{zz}(\alpha) = \sigma_o/2 \ . \tag{30}$$

Since $\bar{\sigma}_{zz}(\alpha)$ is constant for all values of α, a uniform compression of $\sigma_a = -\sigma_o/2$ needs to be applied to obtain the desired plane-displacement boundary conditions. It should be noted that, in contrast to the axisymmetric problem discussed previously, the final axial stress state is not uniform; it depends on α and β. However, the net force is zero and the displacements are plane. Using Hooke's law, the strains resulting from the uniform compression are

$$\begin{aligned}\varepsilon_{\alpha\alpha} = \varepsilon_{\beta\beta} &= \frac{\sigma_o}{4E} \ , \\ \varepsilon_{zz} &= -\frac{\sigma_o}{2E} \ . \end{aligned} \tag{31}$$

So that the changes in the major and minor radii of the channel are

$$\begin{aligned}\Delta a_2 &= \frac{\sigma_o}{4E}a_o \ , \\ \Delta b_2 &= \frac{\sigma_o}{4E}b_o \ . \end{aligned} \tag{32}$$

Combining the results from Eqns. 27 and 32, the total change in the shape of the cross-section of the channel can be found from

$$\begin{aligned}\Delta a_{1-2} &= -\frac{\sigma_o}{2E}a_o \ , \\ \Delta b_{1-2} &= \frac{3\sigma_o}{2E}a_o + \frac{\sigma_o}{E}b_o \ . \end{aligned} \tag{33}$$

The corresponding axial strain resulting from both steps of the calculation is given by

$$\varepsilon_{zz} = -\frac{\sigma_o}{2E} \ . \tag{34}$$

The results of the previous paragraph allow us to calculate the change in volume of the channel. For a slice of length δL_o, the original volume is $V_o = \pi a_o b_o \delta L_o$, where a_o and b_o are the original values of the major and minor radii. The change in volume, ΔV, is given by

$$\frac{\Delta V}{V_o} = \frac{\Delta a}{a_o} + \frac{\Delta b}{b_o} + \frac{\Delta \delta L}{\delta L_o}. \tag{35}$$

Therefore, from Eqns. 33 and 34, the change in volume of the channel associated with the application of a remote tensile stress σ_o is

$$\frac{\Delta V}{V_o} = \frac{3\sigma_o}{2E}\phi_o \ , \tag{36}$$

where $\phi_o = a_o/b_o$ is the initial aspect ratio of the channel.

3.2 Relaxation of applied tension

As with the axisymmetric case, it is assumed that the channel fills with fluid while it is held open by the applied tension. The channel collapses when the applied tension is released, and the fluid flows to the exit. As before, it is assumed that the channel immediately assumes a local equilibrium configuration upon relaxation of the applied tension, such that the interior volume is conserved and there is an initial uniform hydrostatic pressure, P_o, away from the exit. This initial pressure is found following the same procedures as before, using the same assumptions of constant volume, no net axial force, and plane displacements.

The first set of calculations are for plane-strain conditions, with the following boundary conditions:

$$\begin{aligned}
&\sigma_{\alpha\alpha} = -P_o,\ \tau_{\alpha\beta} = 0 \ (\text{at } \alpha = \alpha_o) \ , \\
&\sigma_{\alpha\alpha} = \sigma_{\beta\beta} = \tau_{\alpha\beta} = 0 \ (\text{at } \alpha = \infty) \ , \\
&\varepsilon_{zz} = 0 \ . \qquad (37)
\end{aligned}$$

Wth these boundary conditions, the stresses are [23]

$$\begin{aligned}
\sigma_{\alpha\alpha} &= -\frac{P_o}{4\left(\cosh 2\alpha - \cos 2\beta\right)^2}\left(2\cos 4\beta - 8\cos 2\beta\cosh 2\alpha + 4 + 2e^{-4\alpha} + \frac{\sinh 4\alpha_o}{\sinh 2\alpha_o}2\sinh 2\alpha\right) \ , \\
\sigma_{\beta\beta} &= -\frac{P_o}{4\left(\cosh 2\alpha - \cos 2\beta\right)^2}\left(2\cos 4\beta - 8e^{-2\alpha}\cos 2\beta + 4 + 2e^{-4\alpha} + \frac{\sinh 4\alpha_o}{\sinh 2\alpha_o}2\sinh 2\alpha\right) \ , \\
\tau_{\alpha\beta} &= \frac{P_o}{2\left(\cosh 2\alpha - \cos 2\beta\right)^2}\left(2\sin 2\beta\cosh 2\alpha + \frac{\sinh 4\alpha_o}{\sinh 2\alpha_o}2\sin 2\beta\right) \ , \\
\sigma_{zz} &= -P_o\left(1 - \frac{\sinh 2\alpha}{\cosh 2\alpha - \cos\beta}\right) \ . \qquad (38)
\end{aligned}$$

The changes in major and minor radii of the channel are

$$\begin{aligned}
\Delta a_3 &= \frac{3P_o}{2E}b_o \ , \\
\Delta b_3 &= \frac{3P_o}{2E}a_o \ . \qquad (39)
\end{aligned}$$

The average axial stress for any value of α can be calculated as before:

$$\begin{aligned}
\bar{\sigma}_{zz} &= \frac{1}{\pi/2}\int_0^{\pi/2}\sigma_{zz}d\beta \\
&= \frac{-P_o}{\pi/2}\int_0^{\pi/2}\left(1 - \frac{\sinh 2\alpha}{\cosh 2\alpha - \cos 2\beta}\right)d\beta \\
&= 0 \ . \qquad (40)
\end{aligned}$$

Since there is no axial load arising from the plane-strain calculations, the only additional step required to complete the calculations is the application of a uniform

tensile stress in the solid to provide equilibrium for the compressive force of $P_o \pi a_o b_o$ arising from the hydrostatic pressure in the fluid. However, since a very large substrate has been assumed, the cross-sectional area over which this force is supported is infinite and the magnitude of the axial stress is zero. Therefore, the solution of the previous paragraph is the complete one for this geometry.

Equations 35 and 39 (with $\epsilon_{zz} = 0$) can be combined to find the change in the channel volume resulting from the internal pressure P_o:

$$\frac{\Delta V}{V_o} = \frac{3P_o}{2E}\left(\phi_o + \frac{1}{\phi_o}\right) . \tag{41}$$

Equating this volume change to that given by Eqn. 36, the fluid pressure is found to be

$$P_o = \frac{\phi_o^2}{\phi_o^2 + 1}\sigma_o. \tag{42}$$

This shows that the initial pressure, P_o, is approximately equal to σ_o in cracks ($\phi_0 \to \infty$), and approximately equal to $\sigma_o/2$ in circular channels ($\phi_0 \to 1$). From Eqn. 39 it can be seen that the major and minor radii of the channel after relaxation of the remote tension are

$$\begin{aligned} a &= a_o + \frac{3P_o}{2E} b_o \ , \\ b &= b_o + \frac{3P_o}{2E} a_o \ . \end{aligned} \tag{43}$$

It is important to note that the solutions for the limit of a circular channel are different from those given in the previous section because of the different loading. In the previous section, the channel was opened by an axisymmetric tension. In the present section, the channel is opened by a uniaxial tension.

3.3 Viscous flow in the elliptical channels

The initial pressure in the fluid, P_o, has a value given by Eqn. 42. The difference between this pressure and the ambient pressure at the exit causes the fluid to flow, allowing the channel to collapse. At any position along the channel, the instantaneous pressure is $P(z,t)$. The relationship between the local pressure and the local dimensions of the channel can be derived following the approach used above (see Eqn. 43):

$$\begin{aligned} \frac{\partial a(z,t)}{\partial P(z,t)} &= \frac{3b_o}{2E} \ , \\ \frac{\partial b(z,t)}{\partial P(z,t)} &= \frac{3a_o}{2E} \ . \end{aligned} \tag{44}$$

Alternatively, this allows one to write a relationship between the axes of the ellipse:

$$\frac{\partial a(z,t)}{\partial b(z,t)} = \frac{b_o}{a_o} \ , \tag{45}$$

In addition, Poiuseulle flow in an elliptical pipe has a flow rate of [25]

$$\dot{Q}(z,t) = -\frac{\pi}{4\eta}\frac{\partial P(z,t)}{\partial z}\frac{a^3(z,t)b^3(z,t)}{a^2(z,t)+b^2(z,t)} \ . \tag{46}$$

Finally, the corresponding equation for mass conservation in an elliptical channel is

$$\pi\left[b(z,t)\frac{\partial a(z,t)}{\partial t} + a(z,t)\frac{\partial b(z,t)}{\partial t}\right] = -\frac{\partial \dot{Q}(z,t)}{\partial z} \ . \tag{47}$$

The problem, as defined by equations 43 through 47, can be solved numerically as discussed in the following section. However, an equation with an analytical solution can be established by assuming that $a \approx a_o$ and $b \approx b_o$. With these assumptions, Eqns. 46 and 47 can be re-written as

$$\begin{aligned} \dot{Q}(z,t) &= -\frac{\pi}{4\eta}\frac{\partial P(z,t)}{\partial z}\frac{(a_o b_o)^3}{a_o^2+b_o^2} \ , \\ \pi\left[b_o\frac{\partial a(z,t)}{\partial t} + a_o\frac{\partial b(z,t)}{\partial t}\right] &= -\frac{\partial \dot{Q}(z,t)}{\partial z} \ . \end{aligned} \tag{48}$$

Clearly these equations will not be valid for cracks, when b can open to many multiples of b_o.

Equations 44 and 48 can be combined into two identical, but independent, differential equations for a and b:

$$\begin{aligned} \frac{\partial a}{\partial t} &= \frac{E a_o b_o}{6\eta} \frac{\phi_o^2}{(\phi_o^2+1)^2} \frac{\partial^2 a}{\partial z^2} \\ \frac{\partial b}{\partial t} &= \frac{E a_o b_o}{6\eta} \frac{\phi_o^2}{(\phi_o^2+1)^2} \frac{\partial^2 b}{\partial z^2} \ , \end{aligned} \tag{49}$$

where $\phi_o = a_o/b_o$, as before. It will be noted that when $\phi_o = 1$, these equations are both identical to Eqn. 17 for a tube with an infinite outer radius, and $a = b = R_1$. This suggests a similar normalization to that used in the previous section, with $\tau = Et/\eta$, $\psi_a = a/a_o$, $\psi_b = b/a_o$, and $\zeta = (L_o - z)/a_o$. With this normalization, Eqns. 49 become

$$\frac{\partial \psi_\alpha}{\partial \tau} = \rho^\phi \frac{\partial^2 \psi_\alpha}{\partial \zeta^2} \ ,$$

where $\rho^\phi = \phi_o/6(\phi_o^2+1)^2$, and the subscript α represents a or b, as appropriate. These equations have the same form of solutions as those given in the previous section for the axisymmetric problem. For example, for an infinitely long channel, the sizes of the major and minor axes are given by

$$\psi_\alpha(\zeta, \tau) = 1 + \Delta\psi_\alpha^{max} \ \mathrm{erf}\left(\frac{\zeta}{2\sqrt{\rho^\phi \tau}} \right) \ , \tag{50}$$

where $\Delta\psi_a^{max} = \Delta\psi_b^{max}/\phi_o = 3(\sigma_o/E)\sqrt{3\rho^\phi \phi_o/2}$. The distance at which the dimensions of the cross section have shrunk by 50% is given by the analogue of Eqn. 21:

$$\zeta_{0.5} = 0.954\sqrt{\rho^\phi \tau} \ . \tag{51}$$

Similarly, the solutions for a finite channel follow the form of Eqn. 24.

3.4 Numerical solutions

While an analytical solution can be obtained from the equations given above, the assumption that $b \approx b_o$ becomes increasingly invalid as ϕ_o increases, as can be seen from Eqn 43. In particular, it is not valid for cracks. Although a governing equation for a crack can be derived by assuming that $\partial a/\partial t = 0$ so that $a(t) = a_o$ (see Eqn. 44, in the limit of $b_o = 0$), we were unable to identify an analytical solution for the resulting equation.

Since we were unable to identify analytical solutions for the general problem, we used a numerical approach to solve the original set of equations, without making any assumptions about the aspect ratio. We obtained these numerical solutions by dividing the channel into thin slices of length δL_o, as shown in Fig. 5. We assumed that the j^{th} element was under a uniform pressure, P_j, with a major axis of a_j and a minor axis of b_j. The pressure and the dimensions of the segment were related through Eqn. 44. The pressure gradient in the j^{th} element was $(P_{j+1} - P_j)/\delta L_o$. The volumetric flow rate for each element was determined by Eqn. 46, and the corresponding deformation at each time step was calculated by Eqn. 47. We validated the numerical results by comparing them to the analytical solutions that we knew; there was excellent agreement as will be seen from the plots given in the subsequent sections. Estimates of the numerical uncertainties are indicated on all the accompanying plots; when not visible, they are estimated to be of the order of the line thickness.

4 Discussion

One of the results that can be obtained from the numerical solutions is the velocity at which a collapse front moves into an elastic body. For example, Fig. 6 shows the locations, as function of time, at which the dimensions of a channel have shrunk by a factor of two. It will be noted that the analytical solution given by Eqn. 51 is in excellent agreement with the numerical results, if the aspect ratio is less than about 30. However, while the form of the solution is very similar to that presented earlier for the axisymmetric case, the aspect ratio of an ellipse changes during the collapse, as shown in Fig. 7.

The governing equation for the limiting case of a crack ($a(t) = a_o$, $b_o = 0$) can be derived as

$$\frac{\partial \psi_b}{\partial \tau} = \frac{1}{6} \frac{\psi_b^3}{1 + \psi_b^2} \frac{\partial^2 \psi_b}{\partial \zeta^2} \; . \tag{52}$$

While we have not identified a simple analytical solution to this equation, the numerical results of Fig. 6 suggest that an empirical relationship for the collapse of a crack is

$$\zeta_{0.5} = (6.85 \pm 0.22) \times 10^{-5} \sqrt{\tau} \; . \tag{53}$$

Full numerical solutions for how the dimensions of a crack (with an aspect ratio of 1000:1) change as a function of time are shown in Fig. 8. In particular, the negligible change in the major axis can be seen from Fig. 8(a).

Solutions for the related problem of a fluid entering an initially relaxed channel at an applied pressure P_o can be found by an almost identical analysis. These results might be useful in a totally different application from the one we have focussed on, such as fluids being forced into fissures within rock formations. Although it is not

addressed here, one could imagine coupling these types of results with a fracture criterion for cracks under a hydrostatic pressure. Here, we solve only the problem of channels and cracks opening under the influence of a fluid pressure. To this end, the equations given earlier in the text are solved subject to the following initial and boundary conditions:

$$\begin{aligned} a(0,t) = a(2L_o,t) &= a_o + 3P_o b_o/2E \\ b(0,t) = b(2L_o,t) &= b_o + 3P_o a_o/2E \\ a(z,0) &= a_o \\ b(z,0) &= b_o \ . \end{aligned} \tag{54}$$

The propagation of the opening front (defined as the point at which b is equal to 50% of its maximum value, b^{max}) is shown in Fig. 9. As expected, this is of a similar form to the propagation of a collapse front given in Fig. 6, with limiting results for a circular channel and a crack. Plots of how the channel profile varies along its length at different times are given in Fig. 10. These plots show how the transition between the open portion of the channel and the closed portion of the channel gets sharper as the channel becomes more crack-like. The rapid increase in the opening at the center of the channel corresponds to the point at which the fluid flow from both ends meet.

The original motivation of these analyses was to understand how nano-channels collapse when they are used to linearize DNA and chromosomes [4]. The channels used in those studies were fabricated by tunneling a crack within a thin layer of oxidized PDMS. The channels had a half length of 500 μm, and were opened by different values of applied tension up to 10%. It is believed that the linearization of DNA was facilitated by both the confinement and the flow generated during the narrowing process. Electrical-impedance measurements indicated that the open channels at

10% strain had a cross-sectional area of about 15,000 nm^2 [4]. The size (a_o) of the cracks was difficult to ascertain. However, the calculations in this paper indicate that a strain of 10% would result in a value for b/a_o of 0.15. For an elliptical section, this would correspond of $a_o = 175$ nm, which is not inconsistent with the thickness of the oxidized layer.

Figure 11 shows how the middle of such a channel, with a length of $L_o/a_o = 3000$, collapses as a function of time for different levels of applied strain. This figure shows that there is an incubation time of $\tau_c \approx 1.8 \times 10^6 (\sigma_o/E)^{-3}$, during which the collapse front travels along the channel to the mid-point. The crack then starts to close, eventually reaching a steady-state collapse rate that has an approximate form of $b/a_o \approx 320\tau^{-3}$. If one assumes that the channels are formed in a homogeneous region of PDMS, with a modulus of 3 MPa, and that the fluid is water with a viscosity of 10^{-3} Pa·s, the time is given by $t = 3 \times 10^{-10}\tau$, in seconds. Figure 11 would then indicate that it would take about one second before the center of a channel opened by an applied strain of 10% starts to relax. It was observed experimentally that the rate of collapse of the channels was too fast if the strain was relaxed in one step, so the strain was relaxed in increments of 2 % [4]. This is consistent with the results of Fig. 11 that show the velocity of the crack wall increasing with the initial applied strain. However, the time to relax a strain of only 2% is predicted to be of the order of a minute, rather than a second, as observed. This probably reflects the fact that in the actual experimental configuration, the nano-channels were contained within a layer of oxidized PDMS, rather than within the PDMS itself [4]. The higher modulus of the oxidized material, would result in a smaller time constant. However, the sandwich nature of this experimental geometry is beyond the goal of the present paper.

5 Conclusions

We have developed a model for the time-dependent collapse of liquid-filled channels in elastic bodies. The collapse initiates from the mouth of the channel, and follows the form of a diffusion equation. The characteristic time scale is established as the ratio between the viscosity of the fluid and the modulus of the solid. A collapse front propagates along the channel with a velocity that depends on the distance of the front to the mouth of the channel; its velocity is limited by how quickly the fluid can drain from the channel. An analytical solution can be derived for cylindrical channels; related numerical solutions were determined for elliptical channels. In particular, asymptotic results were obtained for cracks that had been opened up by an applied tension, filled with a fluid, and then allowed to collapse.

The related problem of a channel being opened up by the injection of a fluid under a hydrostatic pressure was also solved. Although the details of the solutions are different, the general form is similar. An opening front propagates along the channel. Crack-like channels exhibit a sharper transition between the open and closed states at the front. An obvious extension to this work might include the effects of a finite toughness, so that the possibility of crack growth, as well as crack opening, could be incorporated.

Acknowledgments

The authors gratefully acknowledge useful discussions with Dr. A. J. Kabla, Prof. K. Garikipati and Prof. W. W. Schultz. The work was supported by the National Institute of Health (R01-HG004653-01), and by the Department of Mechanical Engineering, University of Michigan.

References

[1] K. L. Mills, D. Huh, S. Takayama and M. D. Thouless. Instantaneous fabrication of arrays of normally closed, adjustable, and reversible nanochannels by tunnel cracking. *Lab on a Chip*, 10:1627–1630, 2010.

[2] D. Huh, K. L. Mills, M. D. Thouless and S. Takayama. Tunable elastomeric nanochannels for nanofluidic manipulation. *Nature Materials*, 6:424–428, 2007.

[3] N. Douville, Z. Li, S. Takayama and M. D. Thouless. Crack channelling in a metal-coated elastomer. *Soft Matter*, 7:6493–6500, 2011.

[4] T. Matsuoka, B. C. Kim, J. Huang, N. J. Douville, M.D. Thouless and S. Takayama. Nanoscale squeezing in elastomeric nanochannels for single chromatin linearization. *Nano Letters*, 12:6480–6484, 2012.

[5] X. Zhu, K. L. Mills, P.R. Peters, J. H. Bahng, E. H. Liu, J. Shim, K. Naruse, M. E. Csete, M. D. Thouless and S. Takayama. Fabrication of reconfigurable protein matrices by cracking. *Nature Materials*, 4:403–406, 2005.

[6] A. R. Dixon, C. Moraes, M. E. Csete, M. D. Thouless, M. A. Philbert, and S. Takayama. One-dimensional patterning of cells in silicone wells via compression-induced fracture. *Journal of Biomedical Materials Research Part A*, 2013.

[7] C. Moraes, B. C. Kim, X. Zhu, K. L. Mills, A. R. Dixon, M. D. M. D. Thouless, and S. Takayama. Defined topologically-complex protein matrices to manipulate cell shape via three-dimensional fiber-like patterns. *Lab on a Chip*, 2014.

[8] D. Huh, H. J. Kim, J. P. Fraser, D. E. Shea, M. Khan, A. Bahinski, G. A. Hamilton, and D. E. Ingber. Microfabrication of human organs-on-chips. *Nature Protocols*, 8(11):2135 – 2157, 2013.

[9] J. Huang, B. C. Kim, S. Takayama, and M. D. Thouless. The control of crack arrays in thin films. *Journal of Materials Science*, 49(1):255–268, 2014.

[10] B. C. Kim, T. Matsuoka, C. Morales, J. Huang, M.D. Thouless and S. Takayama. Guided fracture of films on soft substrates to create micro/nano-feature arrays with controlled periodicity. *Scientific Reports*, 3, 2013.

[11] M. C. Cheng, A. T. Leske, T. Matsuoka, B. C. Kim, J. S. Lee, M. A. Burns, S. Takayama, and J. S. Biteen. Super-resolution imaging of pdms nanochannels by single-molecule micelle-assisted blink microscopy. *The Journal of Physical Chemistry B*, 117(16):4406–4411, 2013.

[12] M. Li and J. G. Brasseur. Non-steady peristaltic transport in finite-length tubes. *Journal of Fluid Mechanics*, 248:129–151, 2 1993.

[13] O. Eytan and D. Elad. Analysis of intra-uterine fluid motion induced by uterine contractions. *Bulletin of Mathematical Biology*, 61(2):221–238, 1999.

[14] K. P. Selverov and H. A. Stone. Peristaltically driven channel flows with applications toward micromixing. *Physics of Fluids*, 13(7):1837–1859, 2001.

[15] M. Yi, H. H. Bau, and H. Hu. Peristaltically induced motion in a closed cavity with two vibrating walls. *Physics of Fluids*, 14(1):184–197, 2002.

[16] N. Jeon, D. T. Chiu, C. J. Wargo, H. Wui, I. S. Choi, J. R. Anderson, and G. M. Whitesides. Microfluidics section: Design and fabrication of integrated passive valves and pumps for flexible polymer 3-dimensional microfluidic systems. *Biomedical Microdevices*, 4(2):117–121, 2002.

[17] M. A. Eddings and B. K. Gale. A pdms-based gas permeation pump for on-chip fluid handling in microfluidic devices. *Journal of Micromechanics and Microengineering*, 16(11):2396, 2006.

[18] M. Khoo and L. Chang. A novel micromachined magnetic membrane microfluid pump. In *Engineering in Medicine and Biology Society, 2000. Proceedings of the 22nd Annual International Conference of the IEEE*, volume 3, pages 2394–2397, 2000.

[19] M. A. Unger, H. P. Chou, T. Thorsen, A. Scherer, and S. R. Quake. Monolithic microfabricated valves and pumps by multilayer soft lithography. *Science*, 288(5463):113–116, 2000.

[20] X. Y. Luo and T. J. Pedley. A numerical simulation of steady flow in a 2-d collapsible channel. *Journal of Fluids and Structures*, 9(2):149 – 174, 1995.

[21] A. Marzo, X. Y. Luo, and C. D. Bertram. Three-dimensional collapse and steady flow in thick-walled flexible tubes. *Journal of Fluids and Structures*, 20(6):817 – 835, 2005.

[22] H. S. Carslaw and J.C. Jaeger. *Conduction of heat in solids*. Oxford Science Publications2, 1959.

[23] C. E. Inglis. Stresses in a plate due to the presence of cracks and sharp corners. *Proceedings of the Institute of Naval Architects*, 55:219–230, 1913.

[24] A. Jeffrey and D. Zwillinger. *Table of integrals, series, and products*. Academic Press, 2007.

[25] J. Lekner. Viscous flow through pipes of various cross-sections. *European Journal of Physics*, 28(3):521, 2007.

Figure Captions

Figure 1: Schematic figures of the axisymmetric model. The origin is located at the mid-point of the cylinder. **(a)** A tube has an initial inner radius of R_{1_o}, an initial outer radius of R_{2_o} and an initial half length of L_o. **(b)** Uniform tensile tractions, σ_o, are applied to the outer surface of the tube, resulting in increases in the inner and outer radius. Then, the tube is filled with fluid at the ambient pressure. **(c)** The applied tractions are fully relaxed, resulting in a uniform fluid pressure, $P = P_o$, being established throughout the core. **(d)** The fluid flows out of the tube driven by the difference between the internal fluid pressure, P, and the ambient pressure. The fluid pressure, P, decreases during this process, and its reduction is accompanied by changes in the dimensions of the tube. The tube returns to its original shape as P approaches the ambient pressure.

Figure 2: Profile of the inner surface of a cylindrical channel as a function of distance from the outlet at different times. Plots are shown for an infinitely long channel, and for a channel with $L_o/R_{1_o} = 1000$.

Figure 3: A cartoon based on the analysis showing how a liquid-filled cylindrical tube collapses by Poiseuille from the center of the tube to the exit, when the remote tractions are removed. (The shape change and dimensions are exaggerated, and do not reflect real data.)

Figure 4: **(a)** The elliptical channel has initial radii of a_o and b_o. **(b)** A remote tension of σ_o is applied to open the channel, increasing its size. While the channel is held open, it is filled with fluid at the ambient pressure.

(c) The applied tension is relaxed to zero, resulting in a fluid pressure of P_o. The dimensions of the channel are related to those in (b) by the conservation of volume for an incompressible fluid. This is the initial state from which flow occurs. **(d)** The pressure relaxes back to the ambient pressure as the fluid flows out of the channel to restore the original shape. (The dimensions in the schematics are exaggerated for ease of visualization, and are not to scale.)

Figure 5: A schematic showing the model used in the numerical calculations for deformation of an elliptical channel. A long channel is segmented into thin slices. Each slice has a length of δL_o, and the j^{th} element has a major axis of a_j, a minor axis of b_j, and a pressure of P_j. The values of a_j and b_j are related by Eqn. 44, while Eqns. 46 and 47 are used to calculate the evolution of the channel profile.

Figure 6: A collapse front defined by $\Delta\psi/\Delta\psi_{\max} = 50\%$ travels from the exit of the channel towards the center. Numerical solutions for the position of the collapse front as a function of time are given in this figure. The error bars are comparable with the thickness of the lines. When the original aspect ratio is less than about 30, the motion of the collapse front is described accurately by the analytical solution given in the text. As the aspect ratio increases, the front moves increasingly slowly. However, the numerical solutions suggest there is an asymptotic solution appropriate for cracks ($\phi_o \to \infty$).

Figure 7: The change in aspect ratio along an elliptical channel with an initial aspect ratio of 100, at different times.

Figure 8: **(a)** The relative expansion of the major axis of a crack as a function

of position, at different times after relaxation of an applied strain. **(b)** The relative expansion of the minor axis of a crack as a function of position, at different times after relaxation of an applied strain

Figure 9: An expansion front, defined by the point where b is equal to 50% of its maximum value, b^{max}, travels from the entrance of a channel under a pressure P_o. Numerical solutions for the position of this expansion front as a function of time are given in this figure for very long channels with different aspect ratios.

Figure 10: **(a)** The relative expansion of a cylindrical channel in an infinite substrate as a function of position, at different times after being opened by a fluid under a pressure P_o. **(b)** The relative expansion of the minor axis of an elliptical channel in an infinite substrate with an aspect ratio of 100, as a function of position, at different times after being opened by a fluid under a pressure P_o. **(c)** The relative opening of a crack in an infinite substrate as a function of position, at different times after being opened by a fluid under a pressure P_o.

Figure 11: The width at the center of a long crack, as a function of time and different initial strains. There is an incubation period while the collapse front travels along the channel. This incubation period decreases with the initial strain, and has the approximate form of $\tau_c \approx 1.8 \times 10^6 (\sigma_o/E)^{-3}$. Once the crack has started to collapse, its width follows an approximate form of $b/a_o \approx 320\tau^{-3}$.

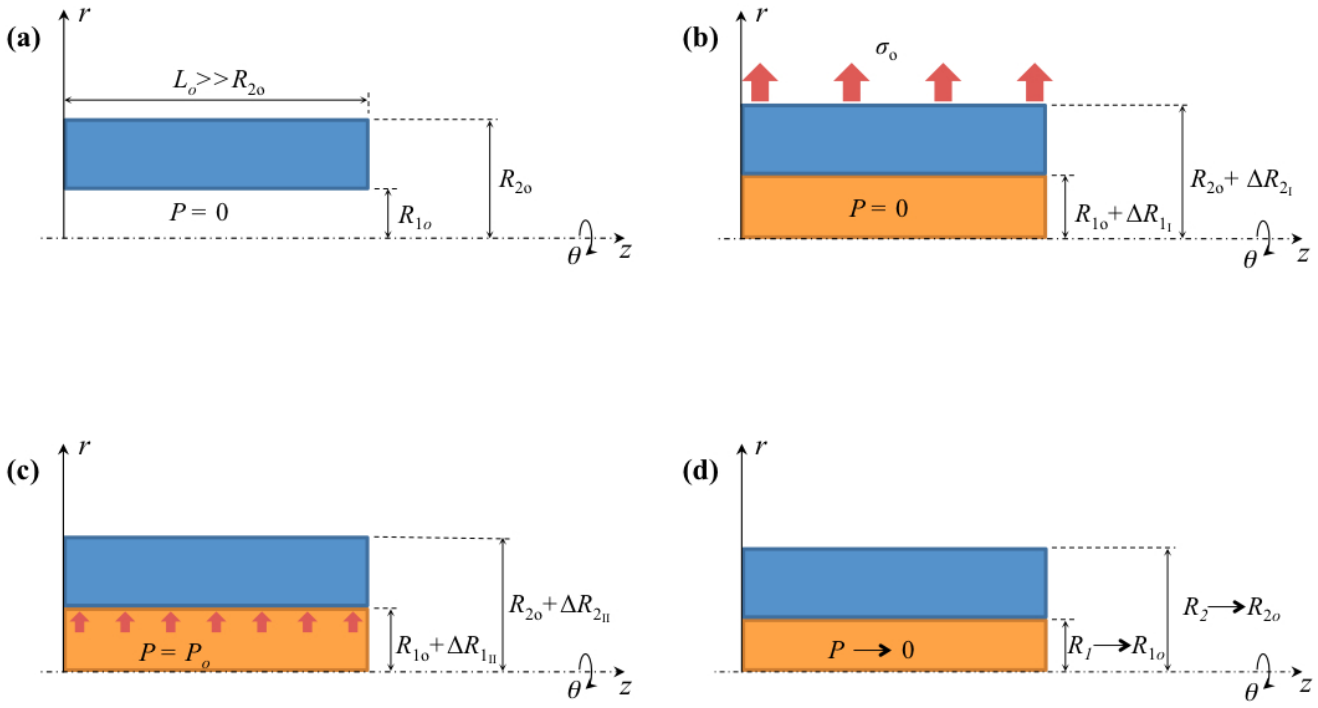

Figure 1: Schematic figures of the axisymmetric model. The origin is located at the mid-point of the cylinder. **(a)** A tube has an initial inner radius of R_{1_o}, an initial outer radius of R_{2_o} and an initial half length of L_o. **(b)** Uniform tensile tractions, σ_o, are applied to the outer surface of the tube, resulting in increases in the inner and outer radius. Then, the tube is filled with fluid at the ambient pressure. **(c)** The applied tractions are fully relaxed, resulting in a uniform fluid pressure, $P = P_o$, being established throughout the core. **(d)** The fluid flows out of the tube driven by the difference between the internal fluid pressure, P, and the ambient pressure. The fluid pressure, P, decreases during this process, and its reduction is accompanied by changes in the dimensions of the tube. The tube returns to its original shape as P approaches the ambient pressure.

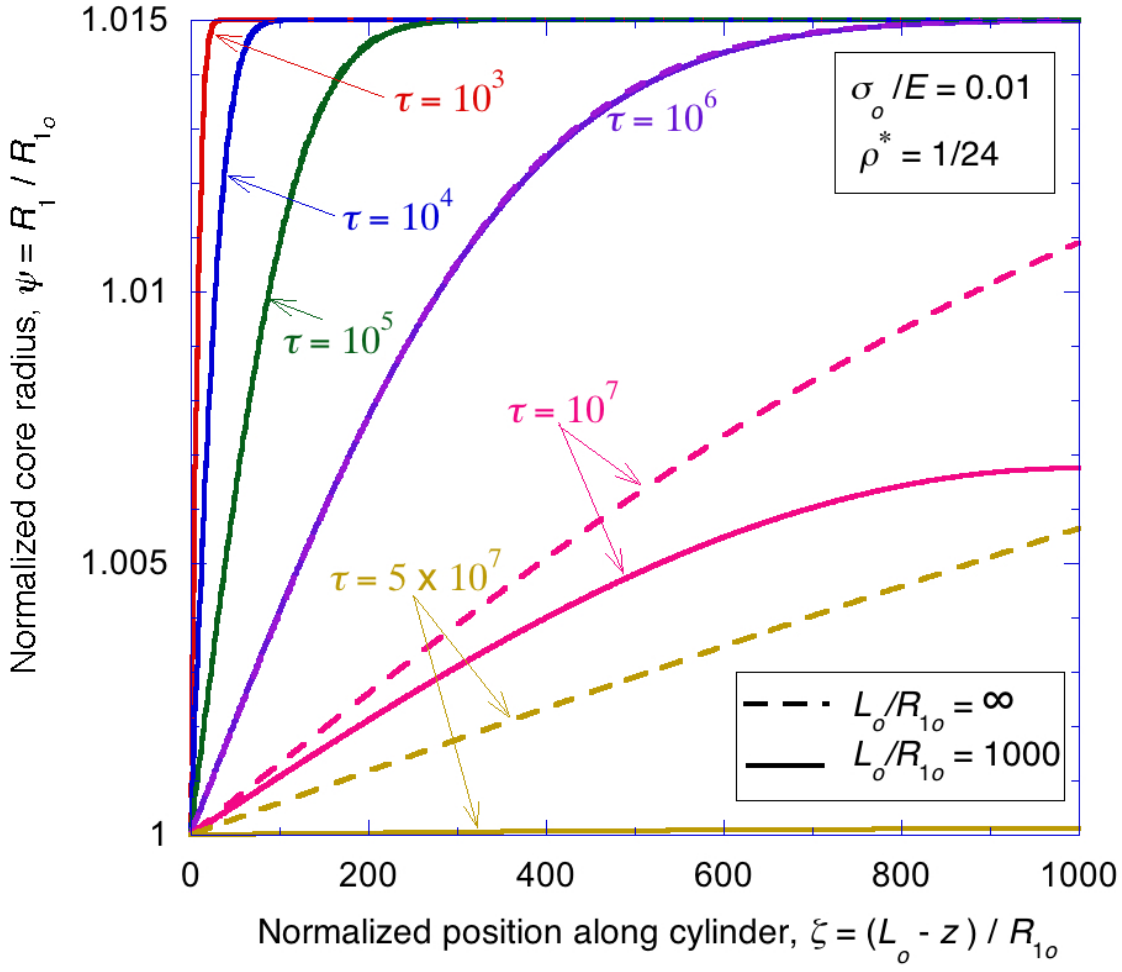

Figure 2: Profile of the inner surface of a cylindrical channel as a function of distance from the outlet at different times. Plots are shown for an infinitely long channel, and for a channel with $L_o/R_{1_o} = 1000$.

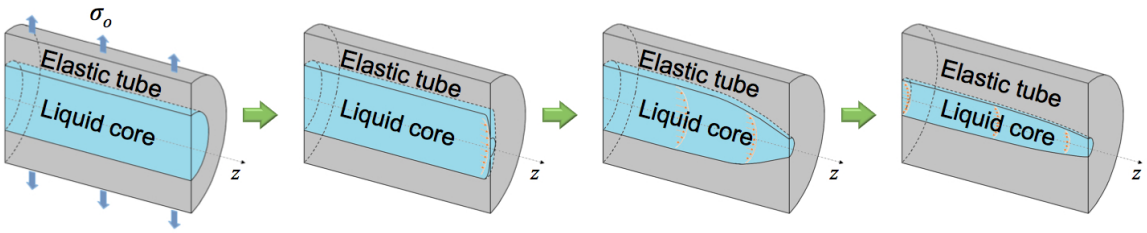

Figure 3: A cartoon based on the analysis showing how a liquid-filled cylindrical tube collapses by Poiseuille from the center of the tube to the exit, when the remote tractions are removed. (The shape change and dimensions are exaggerated, and do not reflect real data.)

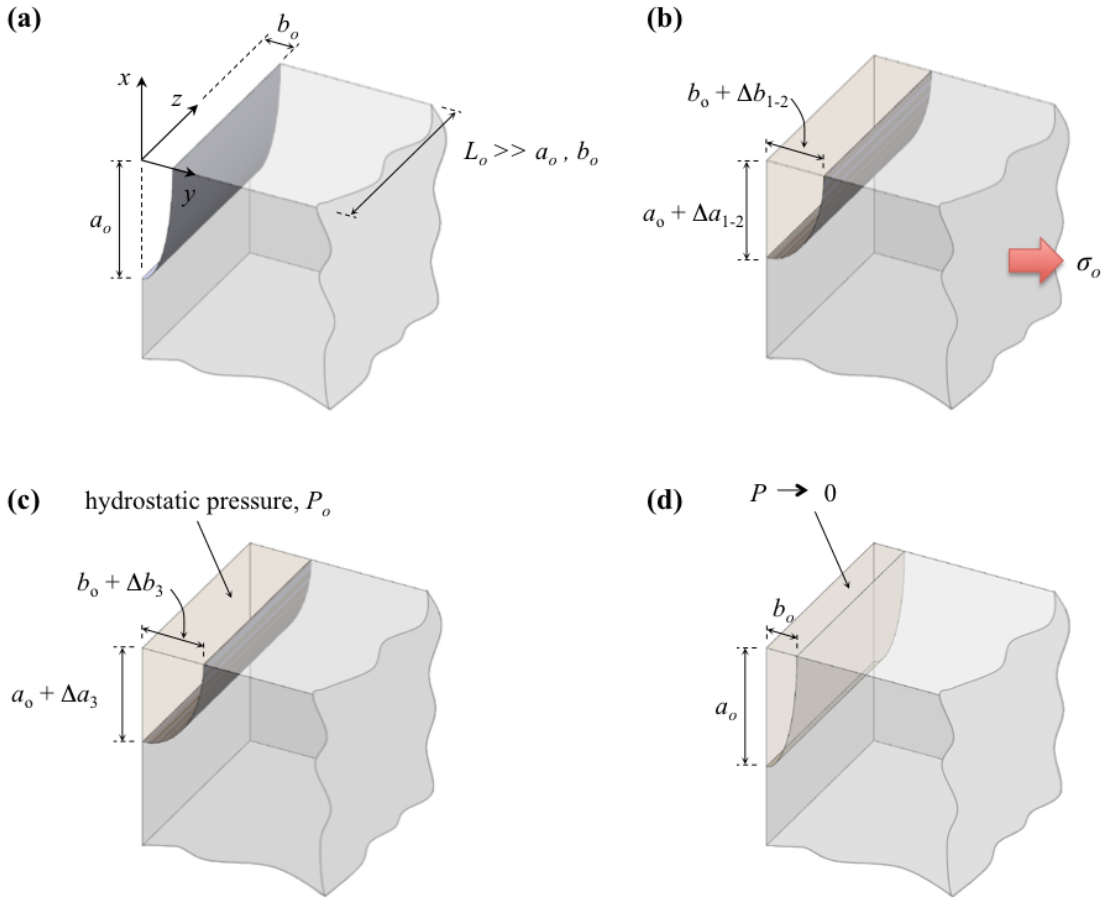

Figure 4: **(a)** The elliptical channel has initial radii of a_o and b_o. **(b)** A remote tension of σ_o is applied to open the channel, increasing its size. While the channel is held open, it is filled with fluid at the ambient pressure. **(c)** The applied tension is relaxed to zero, resulting in a fluid pressure of P_o. The dimensions of the channel are related to those in (b) by the conservation of volume for an incompressible fluid. This is the initial state from which flow occurs. **(d)** The pressure relaxes back to the ambient pressure as the fluid flows out of the channel to restore the original shape. (The dimensions in the schematics are exaggerated for ease of visualization, and are not to scale.)

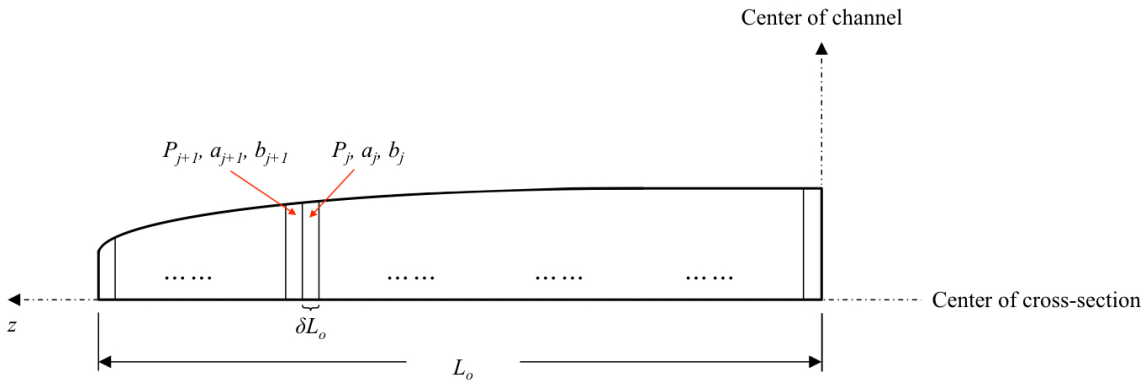

Figure 5: A schematic showing the model used in the numerical calculations for deformation of an elliptical channel. A long channel is segmented into thin slices. Each slice has a length of δL_o, and the j^{th} element has a major axis of a_j, a minor axis of b_j, and a pressure of P_j. The values of a_j and b_j are related by Eqn. 44, while Eqns. 46 and 47 are used to calculate the evolution of the channel profile.

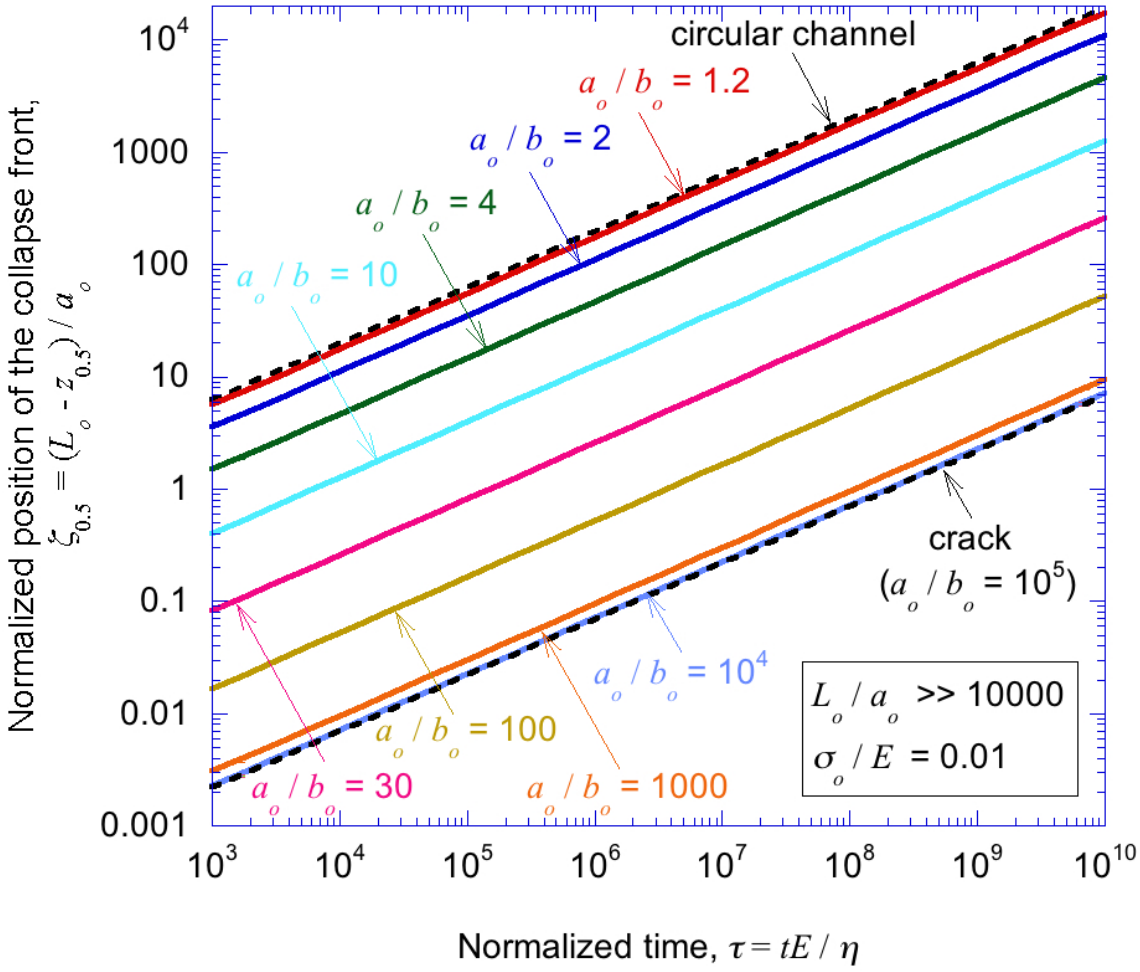

Figure 6: A collapse front defined by $\Delta\psi/\Delta\psi_{\max} = 50\%$ travels from the exit of the channel towards the center. Numerical solutions for the position of the collapse front as a function of time are given in this figure. The error bars are comparable with the thickness of the lines. When the original aspect ratio is less than about 30, the motion of the collapse front is described accurately by the analytical solution given in the text. As the aspect ratio increases, the front moves increasingly slowly. However, the numerical solutions suggest there is an asymptotic solution appropriate for cracks ($\phi_o \to \infty$).

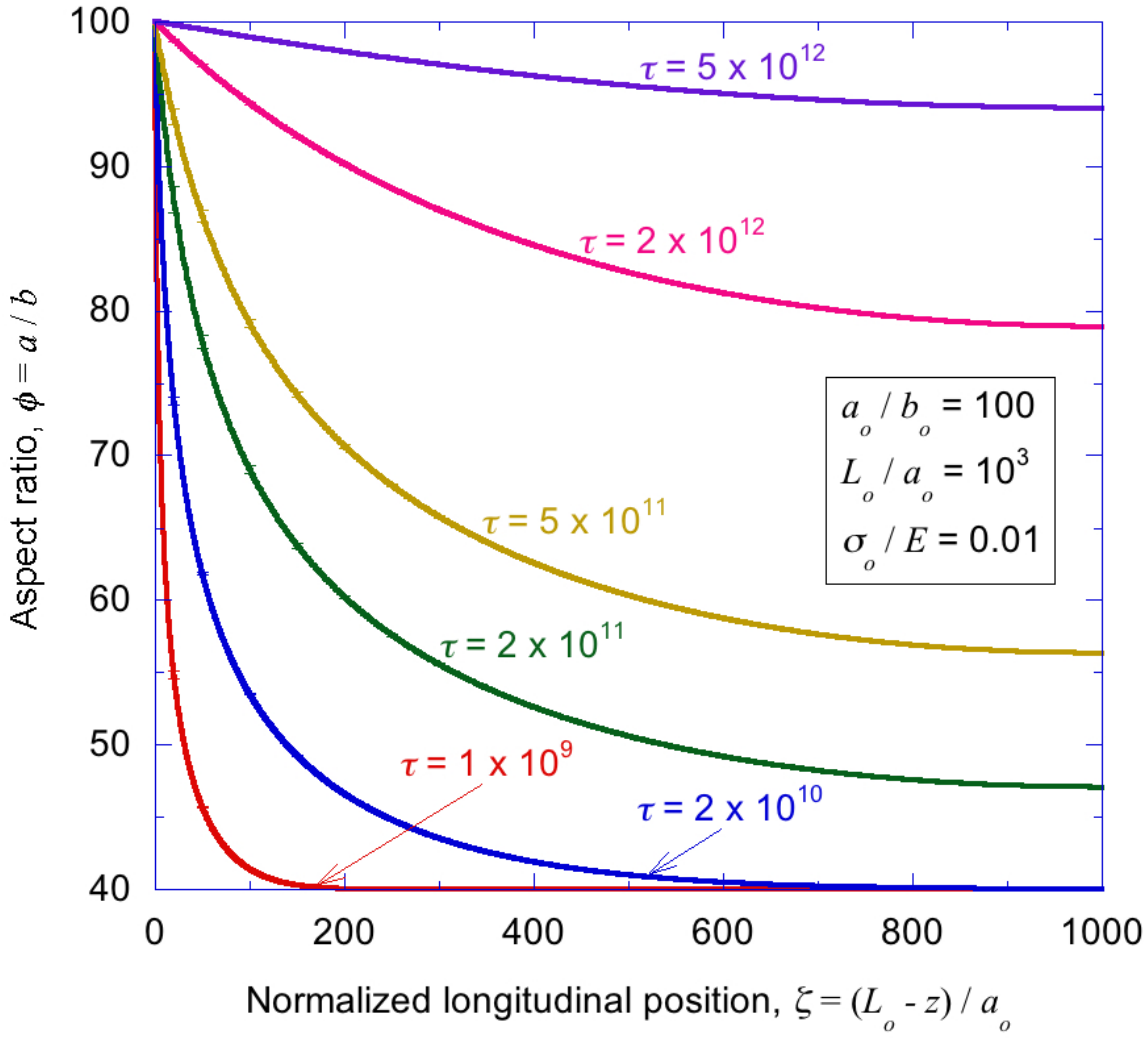

Figure 7: The change in aspect ratio along an elliptical channel with an initial aspect ratio of 100, at different times.

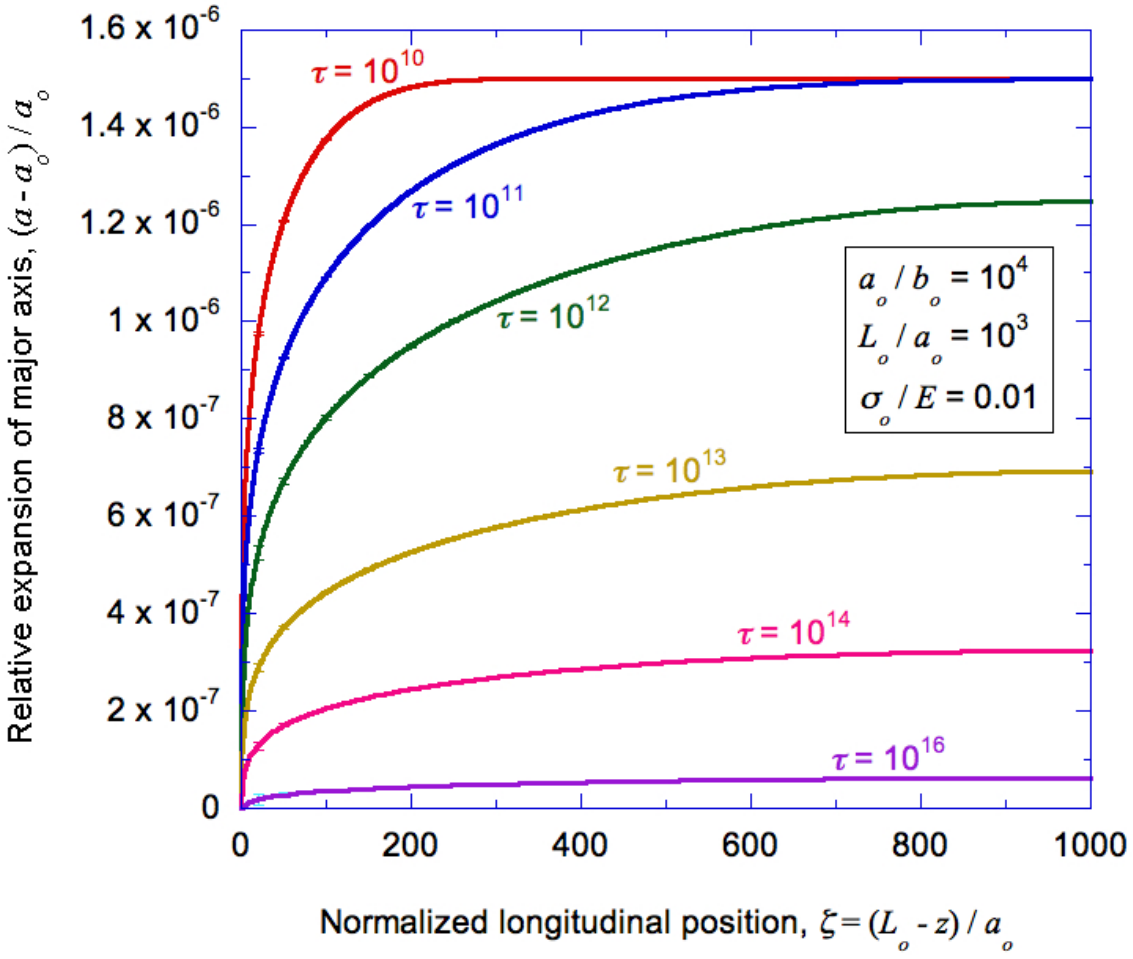

Figure 8: (a) The relative expansion of the major axis of a crack as a function of position, at different times after relaxation of an applied strain.

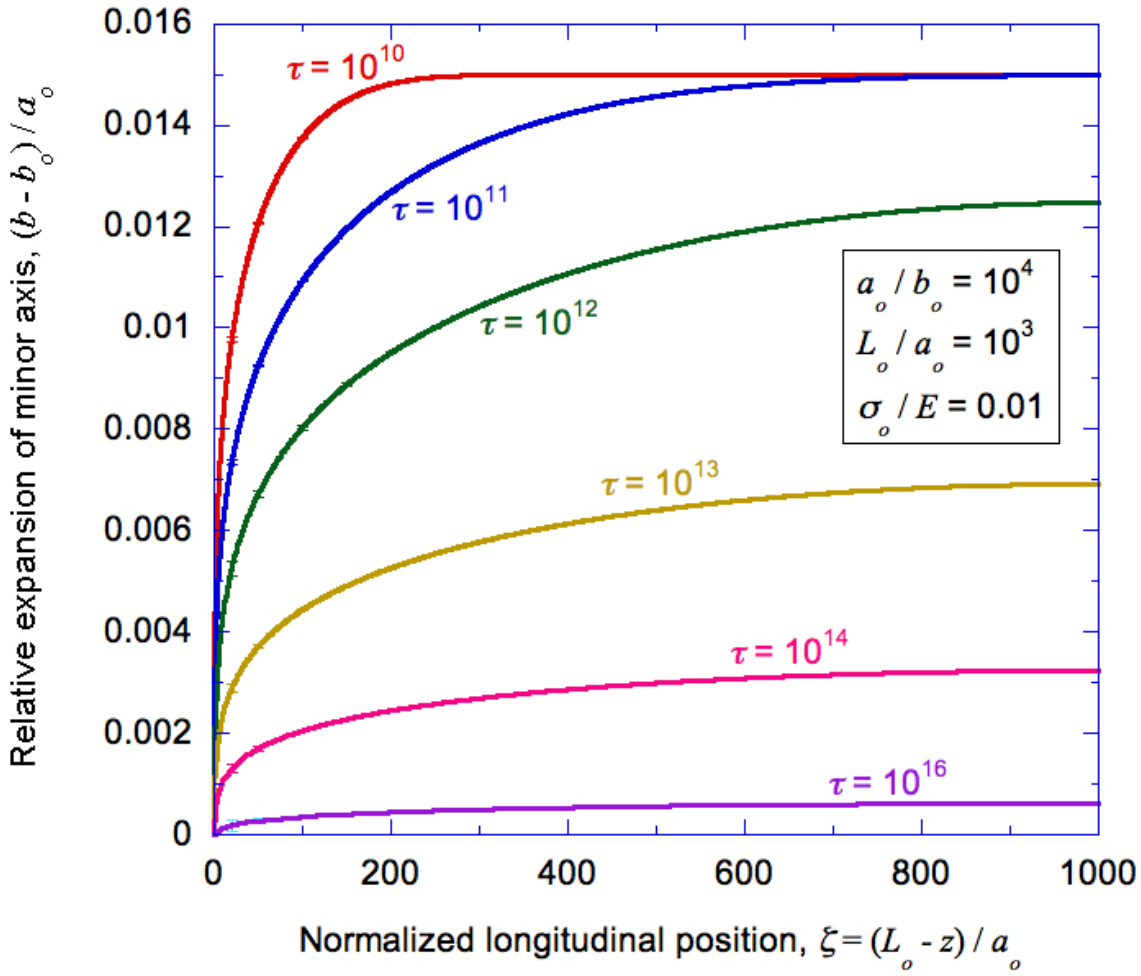

Figure 8: (b) The relative expansion of the minor axis of a crack as a function of position, at different times after relaxation of an applied strain.

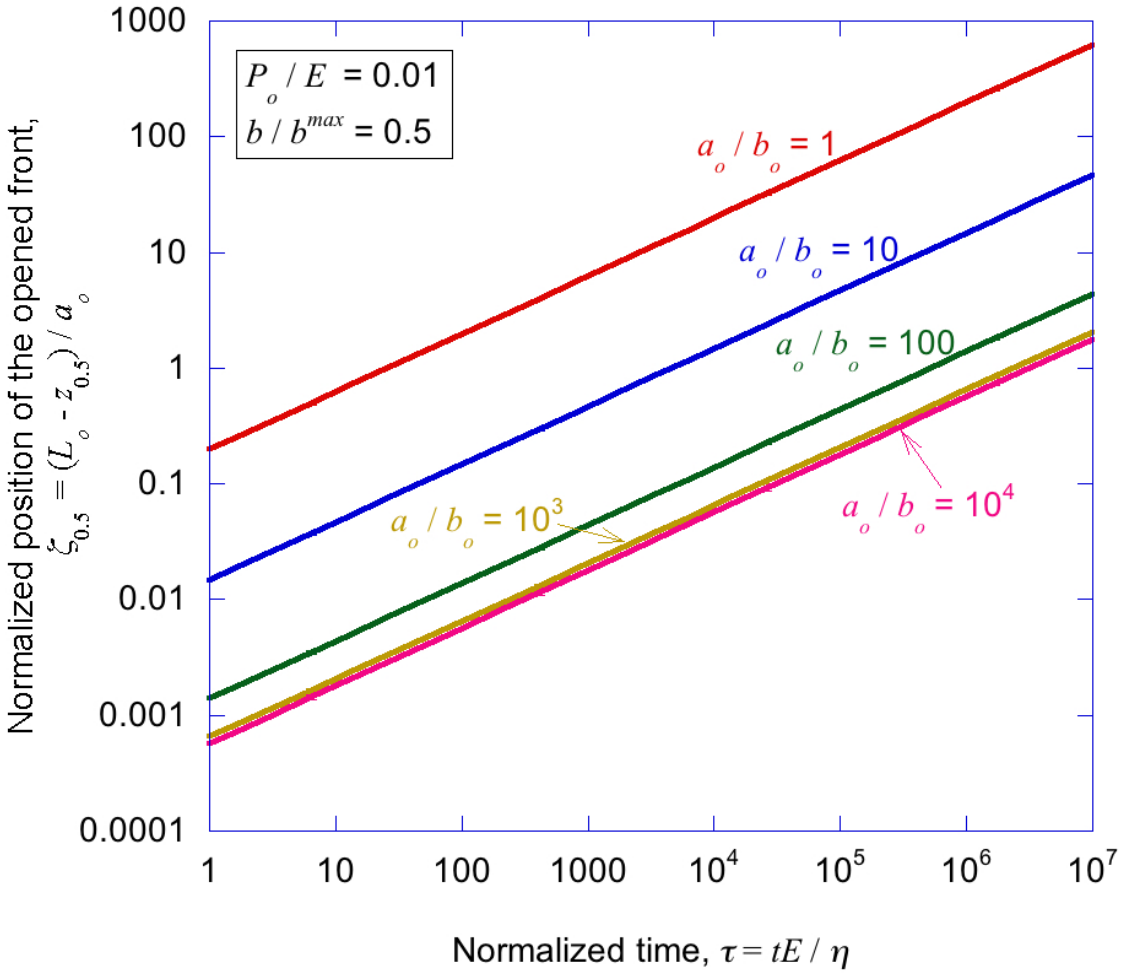

Figure 9: An expansion front, defined by the point where b is equal to 50% of its maximum value, b^{max}, travels from the entrance of a channel under a pressure P_o. Numerical solutions for the position of this expansion front as a function of time are given in this figure for very long channels with different aspect ratios.

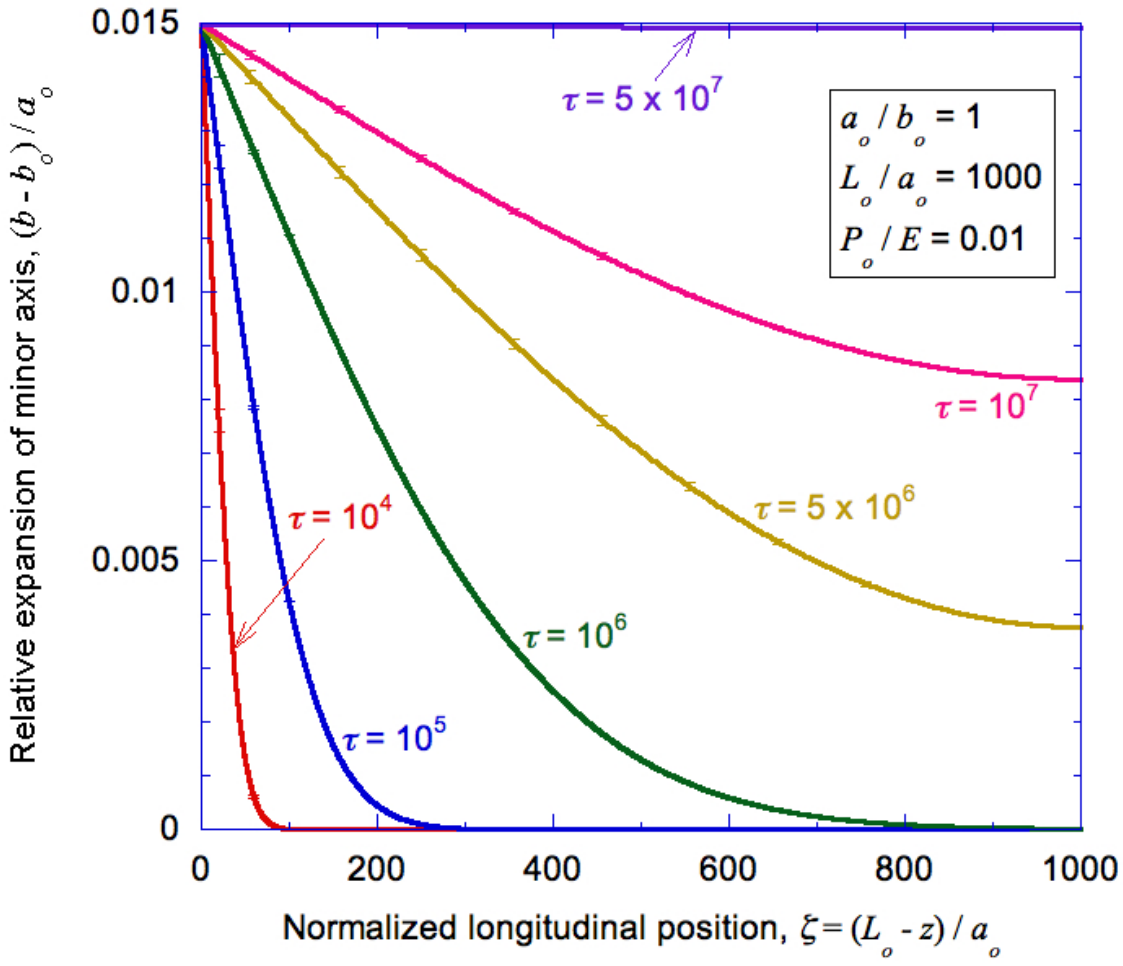

Figure 10: (a) The relative expansion of a cylindrical channel in an infinite substrate as a function of position, at different times after being opened by a fluid under a pressure P_o.

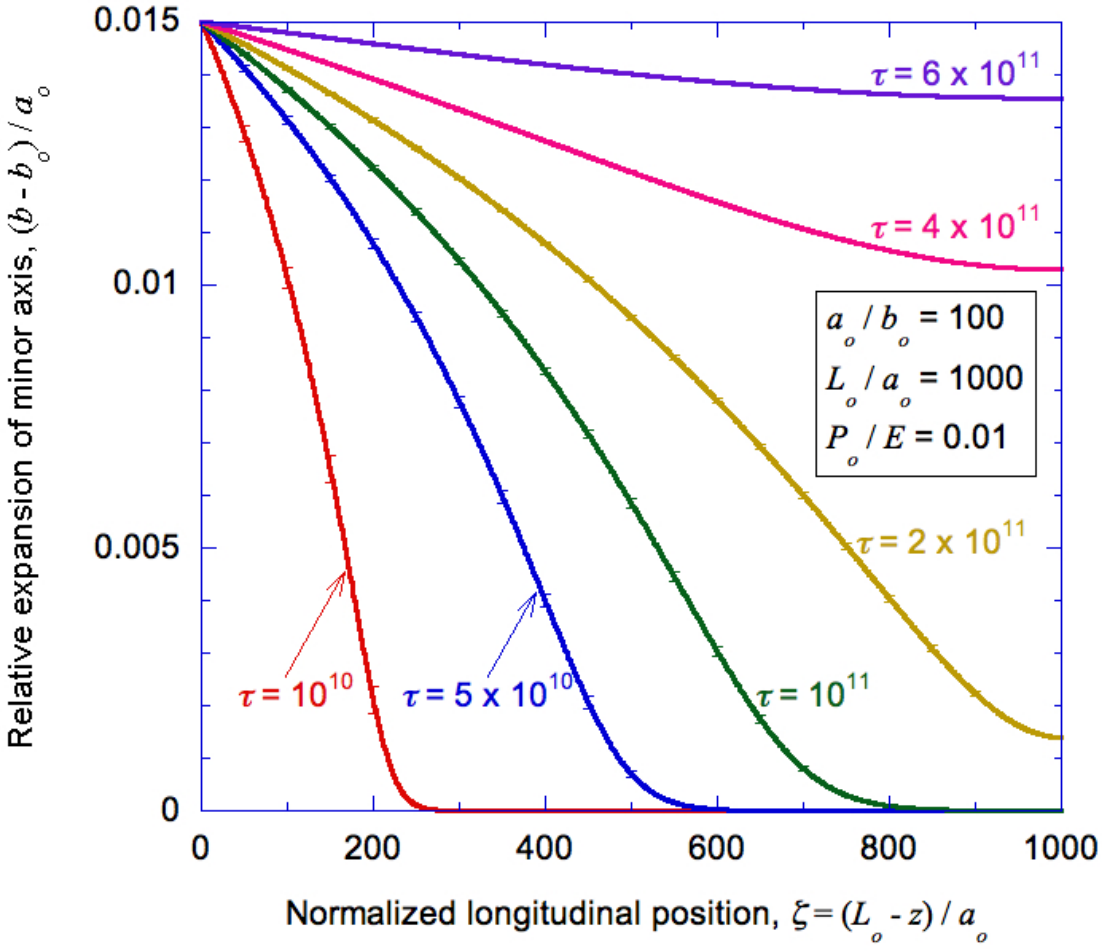

Figure 10: (b) The relative expansion of the minor axis of an elliptical channel in an infinite substrate with an aspect ratio of 100, as a function of position, at different times after being opened by a fluid under a pressure P_o.

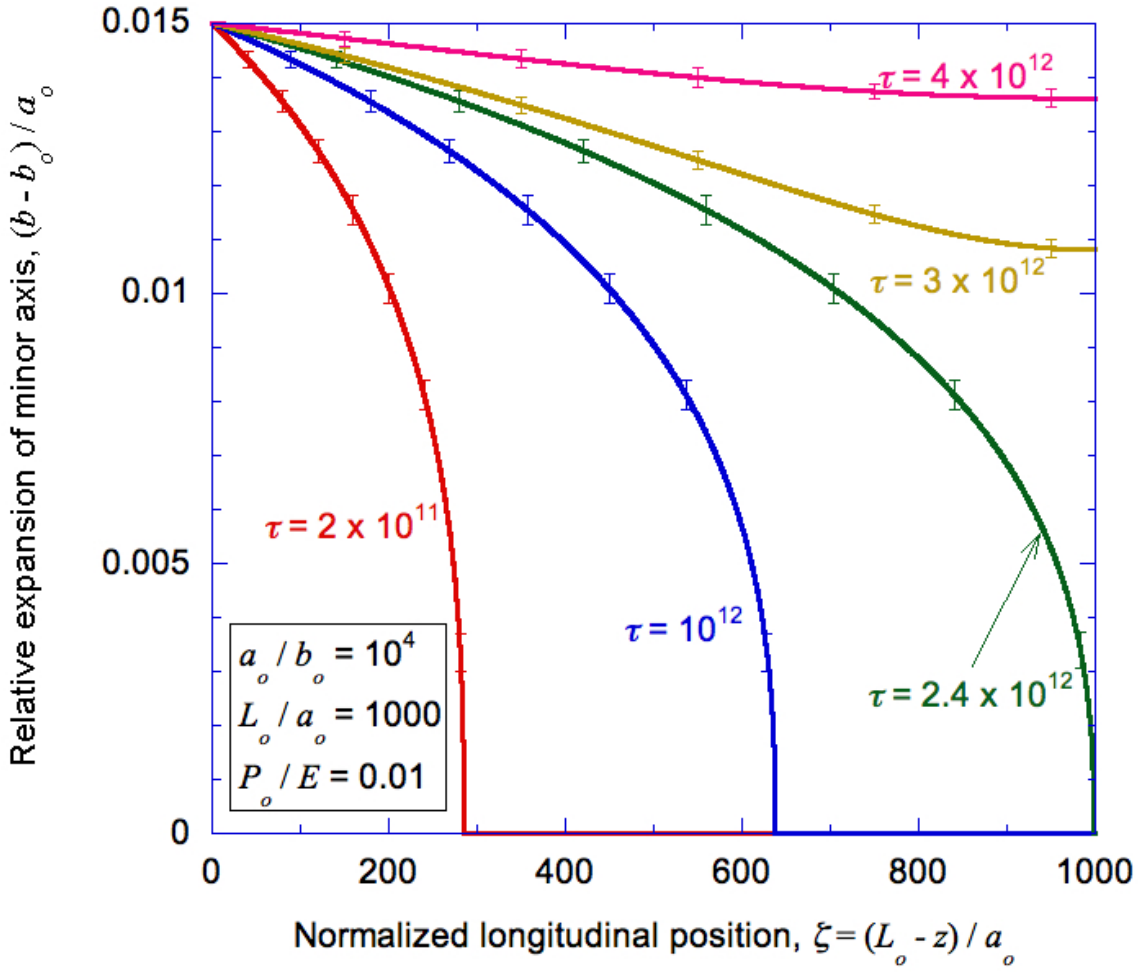

Figure 10: (c) The relative opening of a crack in an infinite substrate as a function of position, at different times after being opened by a fluid under a pressure P_o.

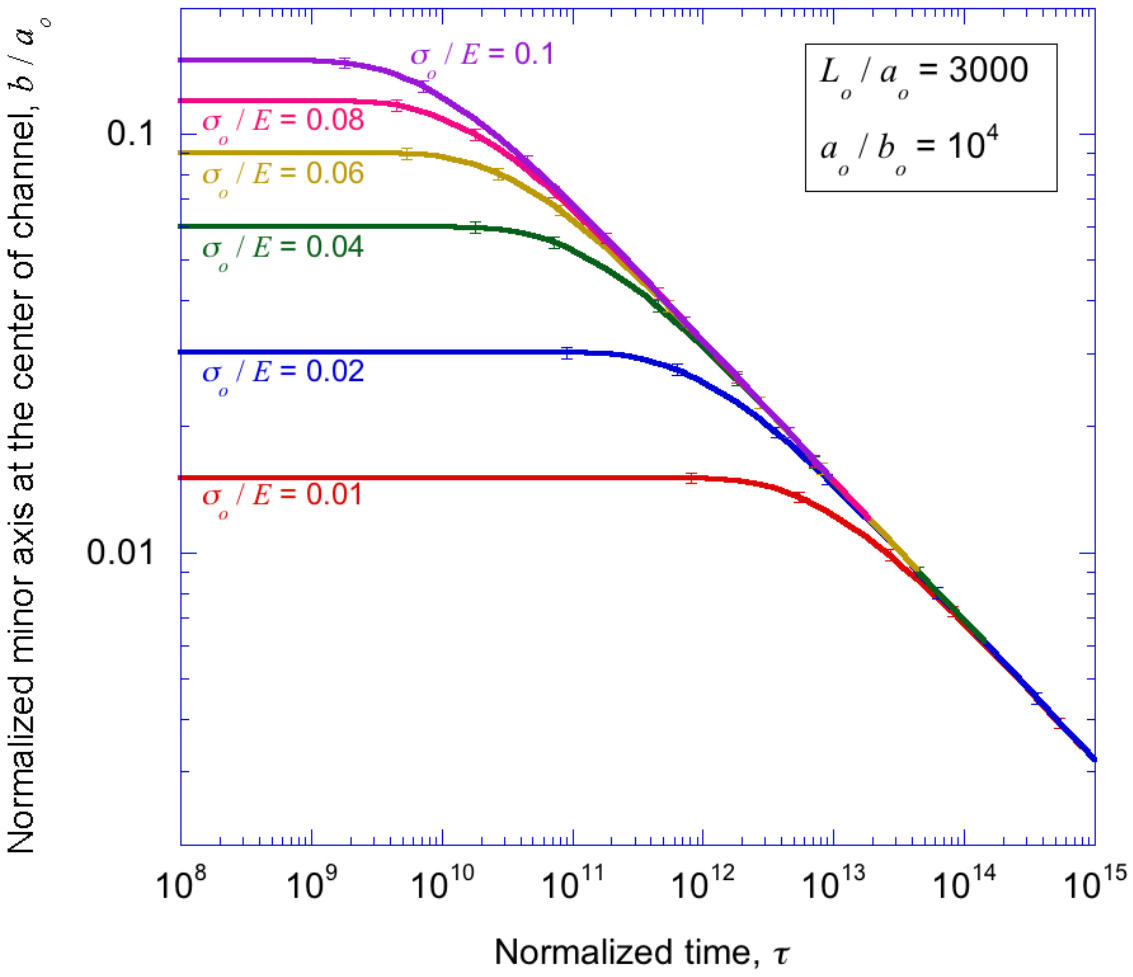

Figure 11: The width at the center of a long crack, as a function of time and different initial strains. There is an incubation period while the collapse front travels along the channel. This incubation period decreases with the initial strain, and has the approximate form of $\tau_c \approx 1.8 \times 10^6 (\sigma_o/E)^{-3}$. Once the crack has started to collapse, its width follows an approximate form of $b/a_o \approx 320\tau^{-3}$.